doi:10.1038/nature13870

Vibrational spectroscopy in the electron microscope

Ondrej L. Krivanek[1,2], Tracy C. Lovejoy[1], Niklas Dellby[1], Toshihiro Aoki[3], R. W. Carpenter[4], Peter Rez[2], Emmanuel Soignard[3,4], Jiangtao Zhu[3]†, Philip E. Batson[5,6], Maureen J. Lagos[5,6], Ray F. Egerton[7] & Peter A. Crozier[8]

Vibrational spectroscopies using infrared radiation[1,2], Raman scattering[3], neutrons[4], low-energy electrons[5] and inelastic electron tunnelling[6] are powerful techniques that can analyse bonding arrangements, identify chemical compounds and probe many other important properties of materials. The spatial resolution of these spectroscopies is typically one micrometre or more, although it can reach a few tens of nanometres or even a few ångströms when enhanced by the presence of a sharp metallic tip[6,7]. If vibrational spectroscopy could be combined with the spatial resolution and flexibility of the transmission electron microscope, it would open up the study of vibrational modes in many different types of nanostructures. Unfortunately, the energy resolution of electron energy loss spectroscopy performed in the electron microscope has until now been too poor to allow such a combination. Recent developments that have improved the attainable energy resolution of electron energy loss spectroscopy in a scanning transmission electron microscope to around ten millielectronvolts now allow vibrational spectroscopy to be carried out in the electron microscope. Here we describe the innovations responsible for the progress, and present examples of applications in inorganic and organic materials, including the detection of hydrogen. We also demonstrate that the vibrational signal has both high- and low-spatial-resolution components, that the first component can be used to map vibrational features at nanometre-level resolution, and that the second component can be used for analysis carried out with the beam positioned just outside the sample—that is, for 'aloof' spectroscopy that largely avoids radiation damage.

In the past two decades, the performance of electron microscopes has been greatly improved by the introduction of multipole-based aberration correction technology[8–11]. Spatial resolution of better than 0.5 Å is now possible[12] and 1 Å is routine. In the scanning transmission electron microscope (STEM), aberration-corrected optics have also allowed the electron current in an atom-sized probe to be increased by 10× and more. This has led to new performance standards, such as nondestructive resolution and identification of all the atoms in a monolayer sample containing various impurities[13], and electron energy loss spectroscopy (EELS) fine structure studies of individual atoms[14–16]. These successes have given rise to a question: can similar technologies improve the energy resolution of EELS carried out in the electron microscope so that vibrational spectra with key features occurring at 50–500 meV become accessible at high spatial resolution, in a wide variety of samples and sample geometries?

Because of recent progress, we are now able to answer the question in the positive. The progress has taken place on three principal fronts: (1) the energy resolution of EELS carried out in the electron microscope has been improved to around 10 meV; (2) the EELS–STEM instrument has been optimized so that the electron probe incident on the sample contains a current sufficient to perform EELS experiments even when the energy width of the probe is ~10 meV and its size <1 nm; and (3) the tail of the intense zero loss peak (ZLP) in the EELS spectrum has been reduced so that it does not obscure the vibrational features of interest. The innovations responsible for the progress are (1) a monochromator of a new design[17], which is able to reach an energy resolution comparable to the highest resolution attained previously[18,19] in broad-beam systems, and which allows an atom-sized electron probe to be formed; (2) an ultra-bright cold field emission electron gun, a dispersing–undispersing monochromator design, and aberration-corrected optics, which together maximize the intensity of the monochromated electron probe; and (3) increasing the energy dispersion of the spectrometer to 1 meV per channel (and higher), and developing operating modes that minimize ZLP tails due to aberrations and stray scattering. A fuller description of the innovations is provided in Methods. Recent improvements in the stability of the whole system are illustrated in Extended Data Fig. 1.

Figure 1 illustrates how the above developments are revealing spectral features that have long been 'hidden in plain sight' in electron microscopes—obscured by a wide ZLP. Figure 1a shows a ZLP obtained with the monochromator slit nearly closed, with a full-width at half-maximum (FWHM) of 9 meV, compared to an unmonochromated spectrum obtained with the system's energy-selecting slit withdrawn from the beam. Figure 1b shows a spectrum obtained from hexagonal boron nitride (h-BN) with the slit slightly more open, to admit a larger current while keeping the probe size small, at two vertical scales: normalized so that the intensity maximum of the ZLP is equal to 1, and multiplied by 1,000, to show the region of the spectrum from 100 to 200 meV. The spectrum was obtained with an electron beam of about 10 pA current and 1 nm diameter. The strong feature at 173 meV corresponds to the energy of the longitudinal optical (LO) phonon in h-BN at 175 meV (see Methods).

Figure 2 shows vibrational excitations recorded in a range of materials: h-BN, SiO_2, SiC, TiH_2 and epoxy resin. The spectra were acquired using various electron-optical settings and total acquisition times ranging from 5 s to 50 s, as described in Methods. For the TiH_2 spectrum, the beam was about 5 nm outside the sample, in a so-called aloof position, to minimize radiation damage. The resin spectrum was recorded in an angle-resolved mode (see Methods) and came from a sample area of about 400 nm in diameter. The intensity of the vibrational peaks is of the order of 3×10^{-5} to 5×10^{-4} (above background) relative to the ZLP. All the peak energies observed here correspond closely to energies recorded by other vibrational spectroscopies: infrared, Raman, low-energy electron and neutron (as shown in Methods and Extended Data Fig. 2).

The observation of vibrational peaks due to hydrogen in TiH_2 and in the epoxy resin is especially interesting. In TiH_2, hydrogen is mobile and bound only weakly, which results in the relatively low (for hydrogen) vibrational energy of 147 meV. In epoxy resin, hydrogen is mostly bound to carbon, and 360 meV (2,900 cm^{-1}) is a typical C–H stretch vibrational energy[1–3]. Up to now, hydrogen has been essentially invisible in electron microscopes, its presence typically inferred from the modified electron distribution due to the electron it contributes to the sample's electron density distribution. Its unambiguous detection by vibrational spectroscopy promises to provide a general technique for hydrogen

---

[1]Nion Company, 1102 Eighth Street, Kirkland, Washington 98033, USA. [2]Department of Physics, Arizona State University, Tempe, Arizona 85287, USA. [3]LeRoy Eyring Center for Solid State Science, Arizona State University, Tempe, Arizona 85287, USA. [4]Department of Chemistry and Biochemistry, Arizona State University, Tempe, Arizona 85287, USA. [5]Institute for Advanced Materials, Devices and Nanotechnology, Rutgers University, Piscataway, New Jersey 08854, USA. [6]Departments of Physics and Materials Science, Rutgers University, Piscataway, New Jersey 08854, USA. [7]Department of Physics, University of Alberta, Edmonton T6G 2E1, Canada. [8]School for Engineering of Matter, Transport and Energy, Arizona State University, Tempe, Arizona 85287, USA. †Present address: TDK Headway Technologies Incorporated, Milpitas, California 95035, USA.

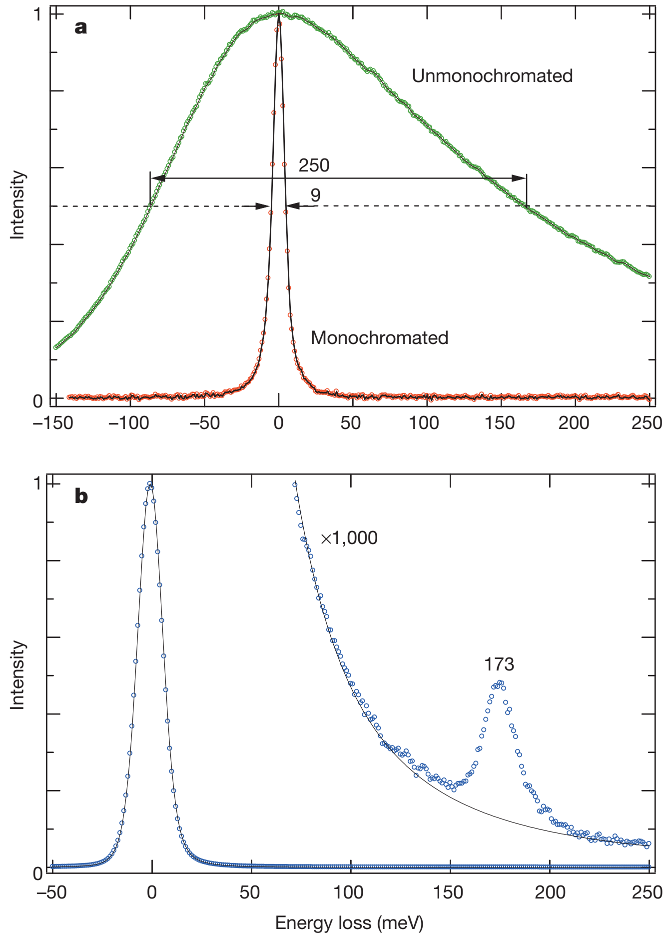

Figure 1 | Revealing vibrational signals in the electron microscope. a, 9 meV wide (full-width at half-maximum, FWHM) monochromated zero loss peak (ZLP) compared to the energy distribution of an unmonochromated beam produced by the system's cold field emission electron gun. **b**, 14 meV wide ZLP obtained with the energy-selecting slit more open (left), and 18 meV wide LO phonon in h-BN, with a peak energy of 173 meV (right).

detection in the many hydrogen-containing materials studied by electron microscopy. Another attractive prospect involves analysing the types of covalent hydrogen bonding present in microscopic amounts of matter, with H–C, H–N, H–O and other types of hydrogen bonds giving distinct vibrational frequencies[1–3].

The width of the vibrational peaks shown in Fig. 2 is 18–40 meV, which is worse than the resolution attainable by other vibrational spectroscopies[1–7]. (The causes of the broadening are discussed in Methods.) However, the main interest of vibrational spectroscopy in an electron microscope lies in studying the spatial variation of vibrational modes in different nanostructures, ideally with near-atomic resolution. With the present energy resolution, the vibrational signal can be distinguished clearly enough to study the spatial variation, and the energy resolution is almost certain to improve further in the future.

Figure 3 explores the spatial resolution of our technique, by imaging the variation of the SiO_2 optical phonon at Si–SiO_2 and SiO_2–vacuum interfaces. A probe of about 2-nm diameter was advanced in 2-nm steps, and a single 10-s spectrum was recorded at each new position. A second scan was performed over the same locations to record the variation of the unsaturated ZLP, and a third scan to record medium-energy EELS losses up to 250 eV, whose strength was used to determine the sample thickness, also shown in the figure. To make sure that the sample did not shift significantly during the profile acquisition and that no significant radiation damage occurred, the examined area was imaged both before and after the spectroscopic line scans, using the high-angle annular dark field (HAADF) signal.

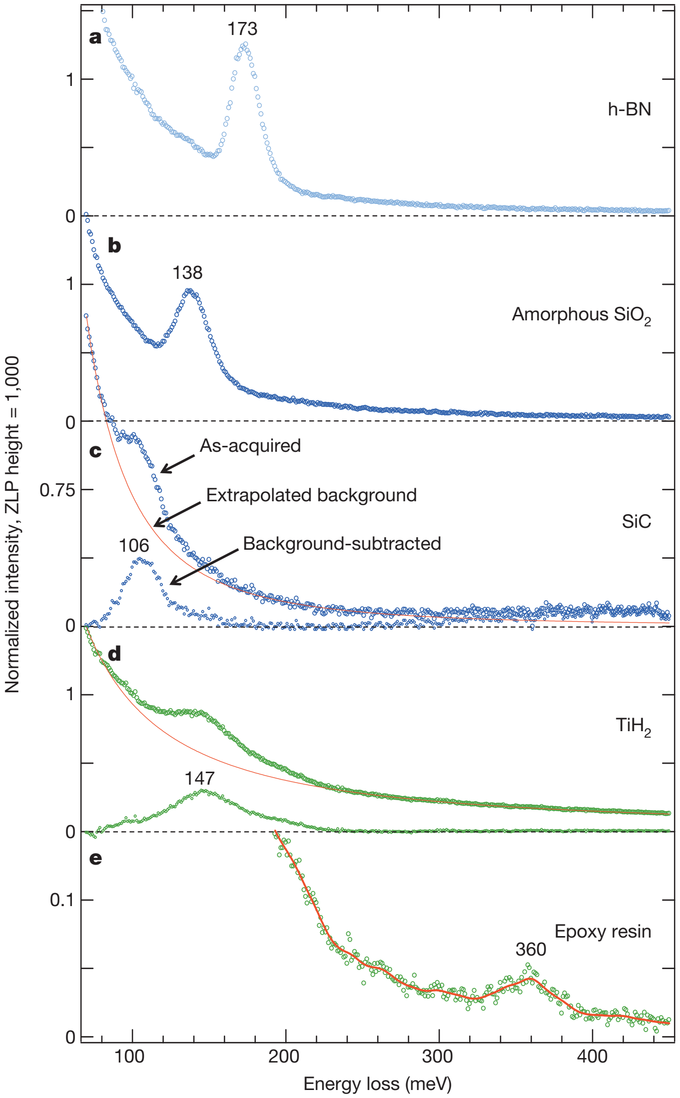

Figure 2 | Vibrational spectra from various materials. a, h-BN; **b**, amorphous SiO_2; **c**, SiC; **d**, TiH_2; and **e**, epoxy resin.

The vibrational signal was obtained by subtracting the background under the peak at 138 meV in all the spectra, which were similar to the spectrum shown in Fig. 2b. The signal was then normalized by dividing it by the intensity of the ZLP. It is seen to extend into the vacuum beyond the edge of the SiO_2 layer, and to decay to 1/e intensity about 40 nm from the edge. The HAADF image and the medium-energy EELS line profile show no such extended feature. This confirms that the spatially extended signal is due to optical phonons being excited even when the electron beam is passing tens of nanometres away from the sample.

Aloof beams losing energy to delocalized electronic excitations (such as surface plasmons) have been studied extensively in low-loss EELS[20–22]. The mechanism can be described by dielectric response theory[23–25]. The probability of excitation varies as $K_0[(2\omega R)/(v\gamma)]$ with the distance R from the specimen (see Methods and Extended Data Fig. 3), where K_0 is a modified Bessel function of the second kind, ω is the excitation frequency, v is the electron velocity and γ is the relativistic (Lorentz) factor. For optical phonon energies of 100–200 meV, this function shows tails extending tens and even hundreds of nanometres with an exponential decay, in good agreement with the present observations.

The spatial resolution obtainable with the aloof signal is comparable to that of tip-enhanced optical spectroscopy[7], without needing to have a sharp tip in the vicinity of the examined structure. Because the interaction distance for the signal can be much larger than the diameter of

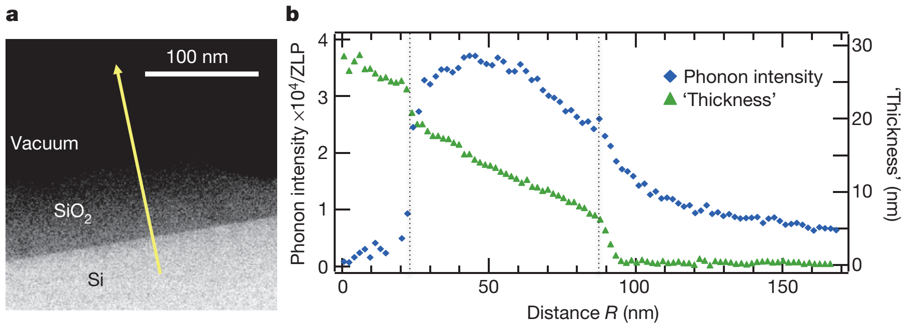

Figure 3 | Profile showing the spatial variation of the vibrational signal. **a**, HAADF image of an Si–SiO_2–vacuum sample viewed in cross-section; the yellow arrow indicates the location of the profile used for **b**. **b**, Net intensity of the SiO_2 vibrational signal (at 138 meV) as a function of the probe position, and approximate sample thickness. The dotted vertical lines mark the locations of the Si–SiO_2 and SiO_2–vacuum interfaces.

the focused probe, the vibrational signal can be collected with the electron beam positioned outside the sample[20–22]. This was in fact done for the titanium hydride spectrum shown in Fig. 2. The 'aloof mode' promises to allow radiation-sensitive materials to be analysed with no (or very limited) ionization and knock-on damage, provided that probe tails are minimized and the flux of electrons directly traversing the sample is negligible. Electrons passing tens of nanometres outside the sample can only cause low-energy excitations, and this means that radiation damage in the aloof mode can be no greater than if the sample were illuminated by infrared light. This will be especially beneficial for materials containing hydrogen, which is very prone to radiation damage due to ionization and knock-on damage by a traversing electron beam.

The spatial variation of the vibrational signal shown in Fig. 3b also includes sharp features that are much narrower than the extended tail. At the SiO_2–vacuum interface, the signal decays to about 70% of the intensity within about 10 nm from the edge, and there is a rapid decay of the vibrational signal within about 5 nm at the SiO_2–Si interface. Recent theoretical estimates suggest that spatial resolutions down to 1 Å should be attainable[26–28] when imaging atomic vibrational states. As discussed in the Methods, the localized signal can be enhanced by selecting only higher-angle scattering events using an annular spectrometer entrance aperture. The cross-section will then be smaller than for the forward-scattered signals used in the present paper, and collecting the spectra will be more challenging experimentally, as it will require combining good energy resolution with large acceptance angles into the spectrometer. Nevertheless, the localized signal is likely to become routinely accessible with further improvements in the experimental technique, leading to a substantial increase in spatial resolution.

Very good spatial resolution should also be obtainable by using impact (Rutherford) scattering[5], which is dominant at high scattering angles ($>$50 mrad), and which can readily result in energy transfers in excess of 50 meV to the nuclei of light elements, especially hydrogen. Energy-analysing the scattering[29] should lead to information similar to that provided by neutron vibrational spectroscopy[4], in principle at the same ångström-scale spatial resolution as HAADF STEM[30], which also utilizes the Rutherford-scattered signal.

In terms of applications, the present technique promises the analysis of vibrational modes at high spatial resolution at structural features such as surfaces, interfaces, grain boundaries, nanotubes and quantum dots. It should also enable electron microscopes to directly detect hydrogen in hydrogen storage materials, polymers and biological tissues. One of the main prospects for the technique is carrying out largely damage-free analysis of radiation-sensitive materials, such as polymers or frozen hydrated biological tissues, using an aloof electron beam. The spatial resolution attained so far is about 5 nm. Future improvements are likely to include electron spectrometers with higher stability and better-corrected optics, which should improve the energy resolution of the technique to below 10 meV and the spatial resolution to below 1 nm. The potential for vibrational spectroscopy in the electron microscope thus appears to be broad and exciting.

Online Content Methods, along with any additional Extended Data display items and Source Data, are available in the online version of the paper; references unique to these sections appear only in the online paper.

Received 9 June; accepted 18 September 2014.

1. Stuart, B. *Infrared Spectroscopy: Fundamentals and Applications* (Wiley, 2004).
2. Griffiths, O. R. & De Haseth, J. A. *Fourier Transform Infrared Spectrometry* 2nd edn (Wiley, 2007).
3. McCreery, R. L. *Raman Spectroscopy for Chemical Analysis* (Wiley, 2000).
4. Mitchell, P. C. H., Parker, S. F., Ramirez-Cuesta, A. J. & Tomkinson, J. *Vibrational Spectroscopy With Neutrons* (World Scientific, 2005).
5. Ibach, H. & Mills, D. L. *Electron Energy Loss Spectroscopy and Surface Vibrations* (Academic, 1982).
6. Stipe, B. C., Rezaei, M. A. & Ho, W. Single molecule vibrational spectroscopy and microscopy. *Science* **280,** 1732–1735 (1998).
7. Dai, S. *et al.* Tunable photon polaritons in atomically thin van der Waals crystals of boron nitride. *Science* **343,** 1125–1129 (2014).
8. Haider, M., Braunshausen, G. & Schwann, E. Correction of the spherical aberration of a 200 kV TEM by means of a hexapole-corrector. *Optik* **99,** 167–179 (1995).
9. Krivanek, O. L., Dellby, N., Spence, A. J., Camps, R. A. & Brown, L. M. Aberration correction in the STEM. *Inst. Phys. Conf. Ser.* **153,** 35–40 (1997).
10. Haider, M. *et al.* Electron microscopy image enhanced. *Nature* **392,** 768–769 (1998).
11. Batson, P. E., Dellby, N. & Krivanek, O. L. Sub-Ångstrom resolution using aberration corrected electron optics. *Nature* **418,** 617–620 (2002).
12. Erni, R., Rossell, M. D., Kisielowski, C. & Dahmen, U. Atomic-resolution imaging with a sub-50-pm electron probe. *Phys Rev. Lett.* **102,** 096101 (2009).
13. Krivanek, O. L. *et al.* Atom-by-atom structural and chemical analysis by annular dark field electron microscopy. *Nature* **464,** 571–574 (2010).
14. Suenaga, K. & Koshino, M. Atom-by-atom spectroscopy at graphene edge. *Nature* **468,** 1088–1090 (2010).
15. Zhou, W. *et al.* Direct determination of the chemical bonding of individual impurities in graphene. *Phys. Rev. Lett.* **109,** 206803 (2012).
16. Ramasse, Q. M. *et al.* Probing the bonding and electronic structure of single atom dopants in graphene with electron energy loss spectroscopy. *Nano Lett.* **13,** 4989–4995 (2013).
17. Krivanek, O. L., Lovejoy, T. C., Dellby, N. & Carpenter, R. W. Monochromated STEM with a 30 meV-wide, atom-sized electron probe. *Microscopy* **62,** 3–21 (2013).
18. Boersch, H., Geiger, J. & Stickel, W. Interaction of 25-keV electrons with lattice vibrations in LiF. Experimental evidence for surface modes of lattice vibration. *Phys. Rev. Lett.* **17,** 379–381 (1966).
19. Terauchi, M., Tanaka, M., Tsuno, K. & Ishida, M. Development of a high energy-resolution electron energy loss spectroscopy microscope. *J. Microsc.* **194,** 203–209 (1999).
20. Walls, M. G. & Howie, A. Dielectric theory of localized energy loss spectroscopy. *Ultramicroscopy* **28,** 40–42 (1989).
21. Cohen, H. *et al.* Near-field electron energy loss spectroscopy of nanoparticles. *Phys. Rev. Lett.* **80,** 782–785 (1998).
22. Garcia de Abajo, F. J. & Howie, A. Electron spectroscopy from outside – aloof beam or near field? *Inst. Phys. Conf. Ser.* **161,** 327–330 (1999).
23. Howie, A. & Milne, R. H. Excitations at interfaces and small particles. *Ultramicroscopy* **18,** 427–4334 (1985).
24. Wang, Z. L. Valence electron excitations and plasmon oscillations in thin films, surfaces, interfaces and small particles. *Micron* **27,** 265–299 (1996).
25. García de Abajo, F. J. Optical excitations in electron microscope. *Rev. Mod. Phys.* **82,** 209–275 (2010).
26. Cueva, P. & Muller, D. A. Atomic-scale optical and vibrational spectroscopy with low loss EELS. *Microsc. Microanal.* **19** (suppl. 2), 1130–1131 (2013).
27. Dwyer, C. Localization of high-energy electron scattering from atomic vibrations. *Phys. Rev. B* **89,** 054103 (2014).
28. Rez, P. Is localised infra red spectroscopy now possible in the electron microscope? *Microsc. Microanal.* **20,** 671–677 (2014).
29. Lovejoy T. C. *et al.* Energy-filtered high-angle dark field mapping of ultra-light elements. *Microsc. Microanal.* **20** (suppl. 3), 558–559 (2014).

30. Pennycook, S. J. & Nellist, P. D. (eds) *Scanning Transmission Electron Microscopy* (Springer, 2011).

Acknowledgements We thank A. Howie and J.-C. Idrobo for discussions, W. J. Bowman, J. Bruley, J. H. Butler, V. Domnich, R. A. Haber, Y. Ikuhara, M. R. Libera, D. S. Lowry and V. Nicolosi for provision of samples, J. Mardinly for help with running the instruments, our co-workers at Nion, especially N. J. Bacon, G. J. Corbin, P. J. Cramer, Z. Dellby, R. W. Hayner, P. Hrncirik, P. Phoungphidok, M. C. Sarahan, G. S. Skone, Z. Szilagyi and T. Yoo for help with the construction of the hardware, electronics and software for HERMES, and C. Trevor of Gatan Inc. for an instability-analysing script. We also acknowledge the use of facilities within the LeRoy Eyring Center for Solid State Science at Arizona State University. Financial support for the purchase of the microscopes was provided by National Science Foundation grants DMR MRI 0821796 (Arizona State University) and DMR MRI-R2 959905 (Rutgers University). Department of Energy grant DE-SC0004954 provided support for P.A.C. and microscopy performed at Arizona State University, and Department of Energy grant DE-SC0005132 provided support for P.E.B., M.J.L. and microscopy performed at Rutgers University. Additional support was provided by the Department of Energy (grant DE-SC0007694), the Natural Sciences and Engineering Council of Canada, the UK Engineering and Physical Research Council (capital equipment grant EP/J021156/1), Arizona State University, Rutgers University and Nion Co.

Author Contributions P.A.C., O.L.K. and P.R. initiated the project, P.A.C., O.L.K. and J.Z. prepared samples, T.A., P.E.B., N.D., O.L.K., M.J.L., T.C.L. and J.Z. obtained electron microscope spectra and images, P.A.C. and E.S. obtained infrared and Raman spectra, T.C.L., N.D., R.F.E. and J.Z. analysed EELS results, P.R. performed theoretical simulations, P.E.B., R.W.C., N.D., R.F.E., O.L.K., T.C.L. and P.R. advised on theoretical interpretation, P.E.B., O.L.K., T.C.L. and E.S. prepared the figures, and O.L.K. and P.R. wrote the paper. All the authors read and commented on the manuscript.

Author Information Reprints and permissions information is available at www.nature.com/reprints. The authors declare competing financial interests: details are available in the online version of the paper. Readers are welcome to comment on the online version of the paper. Correspondence and requests for materials should be addressed to O.L.K. (krivanek@nion.com) or P.A.C. (crozier@asu.edu).

METHODS

Materials and sample preparation. Samples were prepared by crushing and dispersing on holey carbon grids (h-BN, SiC, TiH_2), tripod polishing ($Si–SiO_2$ cross-section) and ultramicrotoming (epoxy resin). In greater detail as follows.

h-BN: As described in ref. 13.

SiC: Fractured powder of mixed SiC polytype. The examined areas had thicknesses of ~0.7 × (mean free path of EELS integrated between 5 and 200 eV).

$Si–SiO_2$–vacuum interface sample: Semiconductor device test structure that was cross-sectioned and thinned using tripod polishing.

TiH_2: TiH_2 powder was crushed between two glass microscope slides and dispersed over a holey carbon film supported on a Cu grid. Smaller particles often failed to show any hydrogen signal, and may have lost their hydrogen during sample preparation. Larger particles (greater than about 0.5 μm in size) showed the hydrogen vibrational signal reliably, and we therefore typically collected spectra from thin areas of larger particles.

Epoxy resin: The sample was a microtomed section of a standard embedding resin used for TEM applications. The resin, obtained from Electron Microscopy Services (catalogue no. 14300), was a low-viscosity epoxy based on a modification of the Spurr resin[31]. The resin was microtomed into sections approximately 100 nm in thickness and supported over a holey carbon film.

Spectrum and image acquisition. Spectra in Figs 1b, 2a, 2b, 2d, 2e and 3 were obtained at Arizona State University with Nion high-energy resolution monochromated EELS systems (HERMES) using a Gatan Enfinium spectrometer; spectra in Figs 1a and 2c were obtained with a HERMES system at Rutgers University using a home-modified spectrometer. Both systems were operated at 60 kV primary voltage, with a beam current incident on the sample of ~10 pA (and a beam current incident on the monochromator slit of ~500 pA), probe convergence semi-angles up to 30 mrad, and EELS collection semi-angles of typically 15 mrad.

The detailed spectrum acquisition times and operating modes used were as listed below. For a more detailed explanation of the HERMES system and its operating modes, see the Methods sections 'Monochromator design' and 'Operating modes'. Figure 1a (monochromated): single acquisition of 10 ms, SR mode with $\alpha = 30$ mrad; Fig. 1b (BN peak): 6 acquisitions of 1 s each, displaced in position to randomize detector pixel variations, and later aligned in energy and summed, SR mode with $\alpha = 30$ mrad; Fig. 2a: single acquisition of 5 s, SR mode with $\alpha = 12$ mrad; Fig. 2b: single acquisition of 15 s, SR mode with $\alpha = 30$ mrad; Fig. 2c: 300 acquisitions of 0.15 s each, displaced in position to randomize detector pixel variations, and later aligned in energy and summed, SR mode with $\alpha = 16$ mrad; Fig. 2d: single acquisition of 10 s, SR mode with $\alpha = 12$ mrad; Fig. 2e: single acquisition of 50 s, AR mode, diameter of the probed sample area ~400 nm, acceptance half-angle ~50 μrad; Fig. 3 and Extended Data Fig. 3: single acquisition of 10 s per probe position, SR mode with $\alpha = 12$ mrad.

All spectra were acquired with an energy dispersion of 1 meV per channel and with a 1 mm diameter EELS entrance aperture. The large dispersion helped to minimize the tail of the ZLP due to sideways spreading of the strong ZLP signal in the scintillator and the fibre optic coupling to the CCDs that detected the spectrum in the spectrometers used here. The images shown in Fig. 3 and Extended Data Fig. 3 were acquired using an HAADF detector spanning detection half-angles of about 80–200 mrad.

Spectrum processing and quantification. Spectra shown in this paper are displayed as-acquired, with no processing except for CCD dark image subtraction and gain normalization. Special care was taken with reference dark and gain images so that so that their statistical noise would not appreciably worsen the noise characteristics of the dark-subtracted and gain-normalized spectra.

The intensities shown in the spatial profiles (Fig. 3 and Extended Data Fig. 3) were extracted by fitting an $a\Delta E^{-r}$ function[32] to the spectrum background next to the peak to be quantified (where ΔE is the energy loss and a and r are adjustable parameters), over a broad energy interval in front of the peak and a narrow interval after the peak. The quality of the fit was checked by examining the background next to the extracted peak and making sure that its intensity was negligible compared to the peak.

The approximate sample 'thickness' t shown in Fig. 3b and Extended Data Fig. 3b was determined by the usual method[32] of computing the thickness from the ratio of the complete EELS intensity I_{total} to the intensity of the ZLP I_{o}, as

$$t = \text{IMFP} \times \ln(I_{\text{total}}/I_{\text{o}})$$

where IMFP is the mean free path for inelastic scattering in the examined material. The energy window used for evaluating I_{total} extended up 250 eV for Fig. 3, and up to 190 eV for Extended Data Fig. 3. IMFP for 60 kV electrons in SiO_2 was computed using the program IMFP.m (ref. 32, appendix B) as 70 nm, IMFP in h-BN as 75 nm. The same IMFP was used for Si as for SiO_2, and the abrupt increase in the approximate thickness seen in Fig. 3b on going from SiO_2 into Si was probably due to IMFP being smaller in Si than in SiO_2.

Monochromator design. Without a monochromator, the attainable energy resolution of EELS carried out in an electron microscope would be limited by the energy width of the electron source to about 0.25 eV for cold field emission (CFE) and 0.5 eV for Schottky sources.

Monochromators employed in electron microscopy have typically been located inside the electron gun, before the electron accelerator. Such an arrangement causes the energy of the electron beam to change whenever instabilities change the high voltage supplied to the electron gun. The end result is a deterioration of the EELS energy resolution, especially for longer acquisition times[33]. The best energy resolution has therefore been reached with systems that compensate for the instabilities by decelerating the electrons before energy analysis, using a high voltage power supply that is shared by the electron gun accelerator and the spectrometer decelerator, so that changes in the high voltage of the gun are precisely compensated in the spectrometer. This type of approach has produced an energy resolution of about 3 meV in a scattering apparatus[18] operating at 30 kV, and 12 meV in a substantially modified electron microscope[19] operating at 60 kV. However, neither of these instruments achieved nm-level spatial resolution, their limits being about 30 μm and 100 nm (at the highest energy resolution), respectively.

The ground-potential monochromator[17] used here employs a stabilization scheme that avoids decelerating the beam but manages to reach comparable energy resolution. It projects an energy-dispersed beam onto an energy-selecting slit using magnetic prisms and multipole optics consisting of about 120 independent optical elements. Because it comes after the accelerator of the electron microscope, the energy it selects does not change when the high voltage supplied to the electron gun changes. The EELS data are acquired using a magnetic prism spectrometer[34,35] that also employs multipole optics. The system's principal stabilization scheme consists of using a shared current supply for powering the magnetic prisms of the monochromator and of the spectrometer, with the principal coils of all the prisms connected in series. This ensures that if the current in the prism coils changes, the EEL spectrum dispersed on the final detector does not move[17,36]. An auxiliary stabilization scheme senses the intensity of the energy-dispersed electron beam incident on the two halves of the energy-selecting slit of the monochromator, and uses the difference signal to adjust the high voltage of the microscope so that the beam remains precisely centred on the slit. The entire system has achieved 3 meV root mean square (r.m.s.) stability at a primary energy of 60 keV, which amounts to a stability of 5 parts in 10^8. This is about a threefold improvement on the stability we were reaching a year ago (Extended Data Fig. 1), and further improvements are expected in the future. The system is also able to achieve a probe size[17] of about 1 Å.

Operating modes. For spectrum acquisition, the STEM–EELS system was operated in two different modes:

(1) SR (spatially resolved) mode, in which there was a focused probe at or near the sample. The probe half-angle α was adjustable (by exciting the condenser lenses differently[37]), and we typically used half-angles from 12 to 30 mrad. To maximize the current in the probe, the current incident on the monochromator slit was typically set to around 500 pA, which was about 2.5× the coherent current[38] I_c of the cold field emission (CFE) source used here. This meant that the minimum attainable probe diameter was about 2× larger than the diffraction-limited probe diameter d_d ($d_d = 0.61\ \lambda/\alpha$, where λ is the electron wavelength). At 60 kV ($\lambda = 4.86$ pm) the $\alpha = 12$ mrad probe therefore had a minimum diameter of 0.5 nm, and the $\alpha = 30$ mrad probe had a minimum diameter of 0.2 nm.

The SR mode is the standard mode of operating a modern STEM: there is a small probe on the sample, and a convergent beam diffraction pattern of adjustable camera length is projected onto the high-angle annular dark field (HAADF) detector and the EELS entrance aperture. The 'EELS entrance object', that is, the beam crossover that is imaged and energy-dispersed by the EELS optics onto the EELS CCD detector, is formed in this mode by the last projector lens of the post-sample optical column[37], P4. If the crossover is too large (or has a pronounced spatially extended tail), it worsens the EELS energy resolution (or adds an energy tail to the ZLP). Therefore, it is useful to keep track of how this crossover is formed, and how the post-sample column aberrations affect its spatial extent. We typically adjusted the post-sample column to give a camera length at the EELS entrance aperture of 33 mm, which meant that a 1 mm diameter EELS aperture accepted half-angles up to 15 mrad, and that the EELS entrance object in the back-focal plane of P4 was an image of the sample-level probe magnified about 15×. For 10 meV energy resolution, entrance crossover diameters of up to about 20 nm could be tolerated, and the above set-up was safely within this limit.

For samples that were moderately sensitive to radiation damage, we typically defocused the sample-level probe to about 2 nm diameter. Much wider areas of the sample could be probed in the SR mode by setting up post-sample descanning such that the beam entering the spectrometer was stationary while the beam at the sample was scanning over large areas.

(2) AR (angle-resolved) mode, in which a large area of the sample was illuminated, and the angular resolution was typically about 300× higher than in the SR mode. The objective lens excitation was kept the same as in the SR mode, and the sample was moved about 16 µm below (upstream of) the objective lens crossover, resulting in about a 400 nm diameter sample area being illuminated when a 12 mrad illumination half-angle was used, and a diffraction pattern of 16 µm camera length being formed in the crossover plane. The projector lenses were adjusted to project a highly magnified (~500,000×) version of this pattern into the entrance aperture plane of the EEL spectrometer, giving a camera length of about 8 m. With the 1 mm EELS entrance aperture that was typically used, this corresponded to an EELS collection half-angle of about 60 µrad. The P4 crossover served once more as the EELS object point. It contained an image of the illuminated sample area, demagnified about 20×. The illuminated area of the sample and the camera length could be varied very flexibly in this mode, simply by moving the sample up/down using the nm-precision *z*-drive of the microscope sample stage. The illumination half-angle of the focused beam inside the objective lens could be varied too, between about 1 and 40 mrad, and this provided additional flexibility. The magnification of the objective lens crossover projected into the EELS aperture plane was always adjusted to illuminate the whole 1 mm aperture. This ensured that the P4 crossover (whose size is inversely proportional to the size of the object projected into the EELS entrance aperture plane) was sufficiently small, so that the size of its image appearing on the spectrometer CCD would not adversely affect the attainable energy resolution.

The AR mode demagnifies a sample level-object to form the EELS entrance object. Haloes formed around the object due to aberrations of the post-sample column or stray scattering from aperture edges, and so on, are demagnified too. As a result, the AR mode is typically able to reduce the tail of the ZLP. It is, however, sensitive to sample charging. The beam is spread on the sample in the AR mode, and sample charging causes a spurious lens effect, which usually varies in time. The spurious lens can distort the shape of the ZLP, causing a loss of energy resolution, as well as an enhancement in the strength of the ZLP tail.

The peak widths of the observed optical phonon features were typically larger than the width of the ZLP. There were several reasons for this, including: (1) integrating over a range of scattering angles and hence over different energy phonons when the phonon energy varied with angle (that is, in the presence of angular dispersion), (2) the finite width of the optical phonon features, and (3) sample charging affecting the resolution in the AR mode as described above. As an example of the second effect, the FWHM of the dominant SiO_2 optical phonon in infrared spectra[39] is about 20 meV, that is, almost the same as the one recorded here.

Infrared, Raman and HREEL spectra of examined materials. Infrared, Raman, high resolution EELS (HREELS) or neutron vibrational spectra are available in the literature for all the materials studied here, with the exception of the epoxy resin. HREELS studies of h-BN using low-energy electrons have identified longitudinal optical (LO), shear (SH) and transverse optical (TO) phonon modes[40], and shown that the dominant LO mode energy varies with the collection angle. For the present collection geometry which emphasized low-angle scattering, the expected LO phonon energy is about 175 meV. SiO_2 has a dominant infrared peak[39] at 1,100 cm^{-1} = 136 meV (to convert cm^{-1} to meV, divide by 8.066), SiC shows a strong infrared absorption peak[41] at 790 cm^{-1} = 98 meV, and TiH_2 gives a dominant peak in neutron vibrational spectra[42] at 150 meV. Except for the SiC spectrum, these all agree with the energies observed in this study to within 3 meV. The SiC energy discrepancy is 8 meV and is probably due to energy differences between different SiC polytypes.

A Raman spectrum from the epoxy resin is shown in Extended Data Fig. 2. It was acquired with an FTIR/FT-Raman spectrometer (Bruker IFS 66V/S) that used a 1,064 nm laser, and the scan covered the range 100–3,500 cm^{-1}. The major peak is centred on 2,920 cm^{-1} = 362 meV, in good agreement with the observed energy of the EELS peak (360 meV).

Theoretical modelling and comparison with experiment. The theory for excitation of localized vibrations by medium energy (30–300 keV) electrons has been given by Dwyer[27] and Rez[28]. The cross-section for the vibrational scattering of 60–100 keV electrons is in the range of 10^3–10^4 barns per atom pair[28], that is, comparable to the integrated cross-sections of EELS inner shell edges, such as the carbon K edge at 284 eV.

The spatial dependence of the signal is well described by the dielectric response to an electron beam moving parallel to a planar interface[23–25]. The scattering probability per unit path length z for an energy loss ΔE is

$$\frac{\mathrm{d}P(R,\omega)}{\mathrm{d}\Delta E\ \mathrm{d}z}=\frac{e^2}{2\pi^2\varepsilon_0\hbar^2v^2}\left\{\mathrm{Im}\left(-\frac{1}{\varepsilon_1(\omega)}\right)\left[\ln\left(\frac{q_c v}{\omega}\right)\right]+K_0\left(\frac{2\omega R}{v\gamma}\right)\left[\mathrm{Im}\left(-\frac{2}{\varepsilon_1(\omega)+\varepsilon_2(\omega)}\right)-\mathrm{Im}\left(-\frac{1}{\varepsilon_1(\omega)}\right)\right]\right\}$$

where R is the distance of the beam from medium 2, ω is the vibration frequency, q_c is a cut-off wave vector, v is the electron velocity in medium 1, $\varepsilon_1(\omega)$ and $\varepsilon_2(\omega)$ are the dielectric functions of media 1 and 2 respectively, and γ is the Lorentz factor. For the aloof beam, medium 1 is a vacuum and $\varepsilon_1(\omega) = 1$. The behaviour with distance from the interface is then given simply by the modified Bessel function of the second kind, K_o, as described in the main text.

A K_o model for the drop-off of the phonon signal with distance R in the vacuum is shown in Extended Data Fig. 3, superimposed on an experimentally measured drop-off in the intensity of the LO optical phonon in h-BN beyond the edge of a BN particle (normalized to the ZLP intensity). The particle thickness, measured by medium-loss EELS (covering an energy interval 5–190 eV), is also shown. The drop-off is probed out to a distance of 300 nm beyond the particle's edge, and the agreement with the K_o function is very good. Because the thickness of the sample was not known accurately, the vertical scaling of the K_o model was adjusted for the best fit. This did not change the predicted relative rate of the signal's decrease with distance.

The sampling interval for the experimental dependence was 20 nm, that is, 10× coarser than for the SiO_2–vacuum interface probed in Fig. 3, and too coarse to fully capture the spatial variation right at the particle's edge. At >100 nm from the sample edge, the phonon tail follows a simple exponential decay, as shown in Extended Data Fig. 3. Closer to the edge of the sample, however, both the observed phonon signal and the K_o function rise to much higher values than an exponential. K_o in fact rises to infinity at $R = 0$, but the singularity is removed in practice by the finite width of the electron probe and by other effects such as high-angle scattering events not being accepted into the spectrometer. The excess signal relative to the exponential corresponds to a 'localized' vibrational signal, and a key question for the future is: how precisely can the localized signal be recorded in the presence of the 'extended' signal?

Accepting only scattering angles greater than a few mrad into the EEL spectrometer, for instance by an annular pre-EELS aperture that blocks the STEM bright field disk, should in principle suppress the extended signal and make the localized signal more visible. Collecting the localized signal efficiently will then require increasing the range of the scattering angles accepted into the spectrometer, while keeping the energy resolution the same (or improving it). This will place higher demands on the quality of the aberration correction in the post-sample part of the optical column and in the spectrometer. Such improvements are expected in the future, especially now that it has become clear that they are likely to lead to a significant increase in the spatial resolution of vibrational spectroscopy in the electron microscope.

31. Spurr, A. R. A low-viscosity epoxy resin embedding medium for electron microscopy. *J. Ultrastruct. Res.* **26,** 31–43 (1969).
32. Egerton, R. F. *Electron Energy Loss Spectroscopy in the Electron Microscope* 3rd edn (Springer, 2011); http://www.tem-eels.ca/computer-programs/index.html.
33. Tiemeijer, P. C., van Lin, J. H. A., Freitag, B. H. & de Jong, A. F. Monochromized 200 kV (S)TEM. *Microsc. Microanal.* **8** (suppl. 2), 70–71 (2012).
34. Krivanek, O. L., Gubbens, A. J., Dellby, N. & Meyer, C. E. Design and first applications of a post-column imaging filter. *Microsc. Microanal. Microstruct.* **3,** 187–199 (1992).
35. Gubbens, A. J. *et al.* The GIF Quantum, a next generation post-column imaging energy filter. *Ultramicroscopy* **110,** 962–970 (2010).
36. Krivanek, O. L. *et al.* Towards sub-10 meV energy resolution STEM-EELS. *Inst. Phys. Conf. Ser.* **522,** 012023 (2014).
37. Krivanek, O. L. *et al.* An electron microscope for the aberration-corrected era. *Ultramicroscopy* **108,** 179–195 (2008).
38. Krivanek, O. L., Chisholm, M. F., Dellby, N. & Murfitt, M. F. in *Scanning Transmission Electron Microscopy: Imaging and Analysis* (eds Pennycook, S. J. & Nellist, P. D.) 613–656 (Springer, 2011).
39. Bock, J. & Gouq-Jen, S. Interpretation of the infrared spectra of fused silica. *J. Am. Ceram. Soc.* **53,** 69–73 (1970).
40. Oshima, C. & Nagashima, A. Ultra-thin epitaxial films of graphite and hexagonal boron nitride on solid surfaces. *J. Phys. Condens. Matter* **9,** 1–20 (1997).
41. Li, P. J. *et al.* Structural characterization of nm SiC films grown on Si. *Appl. Phys. Lett.* **62,** 3135–3137 (1993).
42. Bashkin, I. O. *et al.* Hydrogen interaction and bound multiphonon states in vibrational spectra of titanium hydrides. *Z. Phys. Chem.* **179,** 335–342 (1993).

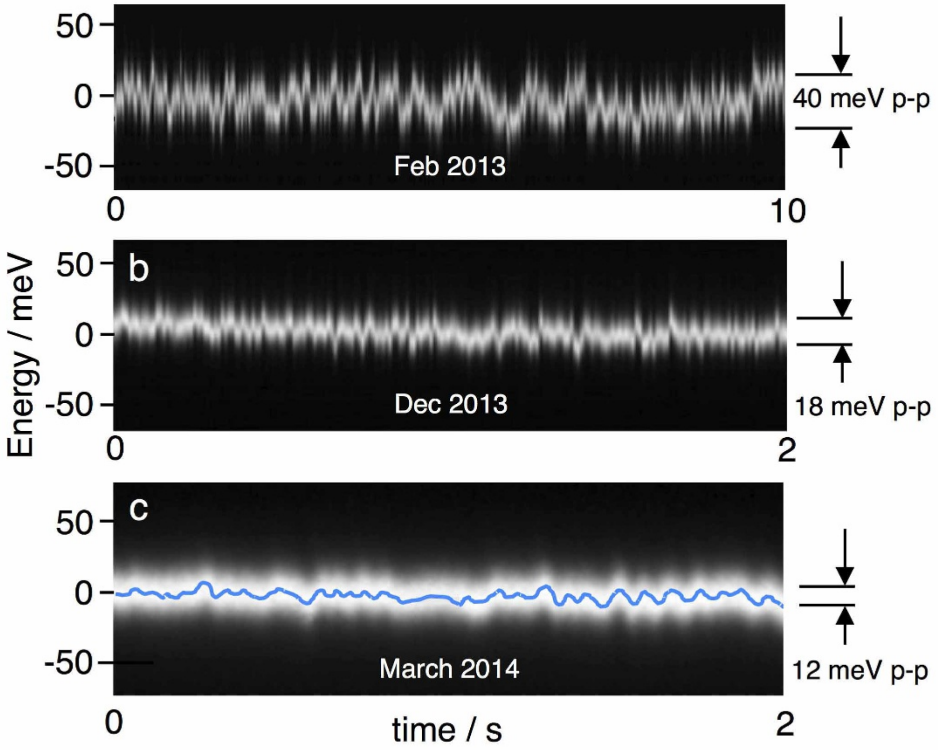

Extended Data Figure 1 | Analysis of total system instabilities, performed by plotting the position of the ZLP on the EEL spectrometer detector as a function of time. **a**, Using the Gatan Enfinium EELS and original power supplies: ~50 meV peak-to-peak and 12 meV r.m.s. instability. **b**, As **a** but with improved-stability power supplies: ~18 meV peak-to-peak and 4.5 meV r.m.s. instability. **c**, Single magnetic sector EELS with Nion power supplies: ~12 meV peak-to-peak and 3 meV r.m.s. instability. Panels **a** and **b** show the position of the ZLP on the EELS detector as a function of time, marking each position of the ZLP with a single point; **c** shows the whole ZLP profile, together with a blue trace that follows the instantaneous position of the centre of the profile.

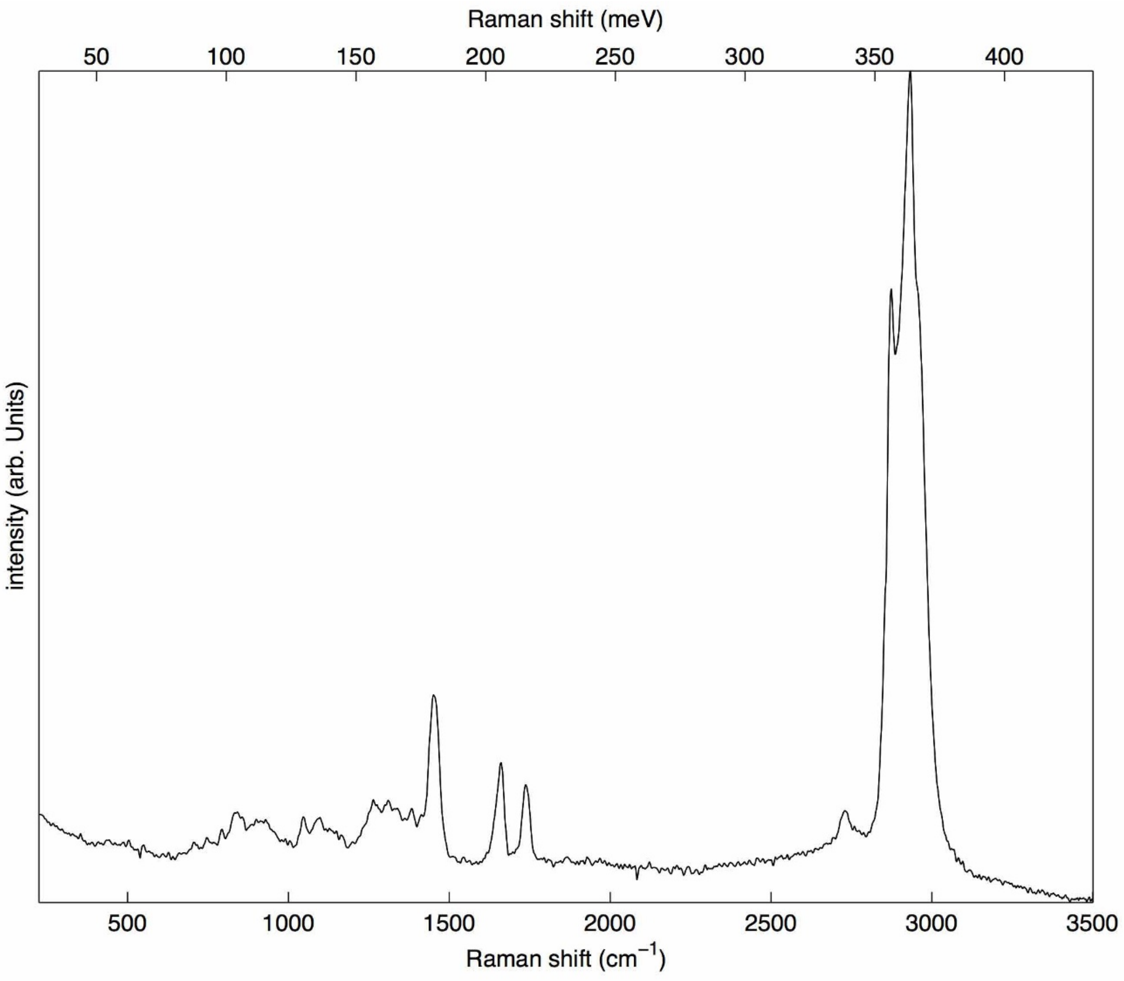

Extended Data Figure 2 | Raman spectrum of epoxy resin. The major peak is centred on 2,920 cm^{-1} = 362 meV.

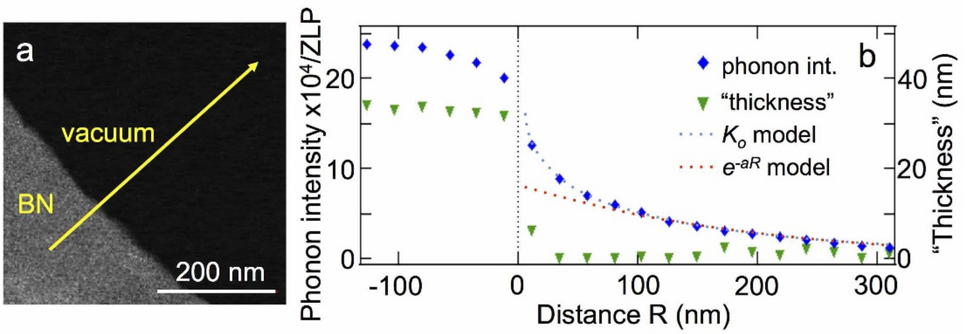

Extended Data Figure 3 | Fall-off of the h-BN LO phonon signal in the vacuum, probed out to 300 nm. **a**, HAADF image of an edge of a BN particle of nearly constant thickness, with the probed line indicated by a yellow arrow. **b**, Shown are the intensity of the BN phonon signal peak (at 173 meV) along the probed line (blue diamonds), the K_o model of the phonon signal decay in vacuum (dotted blue line), the exponential model of the same (dotted red line), and approximate sample thickness (green triangles). The edge of the particle is at $R = 0$.